International Journal of Hydrogen Energy 127 (2025) 51–63

Contents lists available at ScienceDirect

International Journal of Hydrogen Energy

journal homepage: www.elsevier.com/locate/he

Performance data extraction from dynamic long-term operation of proton exchange membrane and alkaline water electrolysis cells

Sharon-Virginia Pape [a,b,1], Sarah Zerressen [a,1,*], Martin Florian Seidler [a,c,1], Roger Keller [a], Felix Lohmann-Richters [a], Martin Müller [a], Ulf-Peter Apfel [d,e], Anna K. Mechler [a,f,g], Andreas Glüsen [a,*]

[a] Forschungszentrum Jülich GmbH, Institute of Energy Technologies, IET-4: Electrochemical Process Engineering, 52425, Jülich, Germany
[b] RWTH Aachen University, Faculty 4, 52062, Aachen, Germany
[c] Forschungszentrum Jülich GmbH, Institute of Energy Materials and Devices, IMD-3: Photovoltaics, 52425, Jülich, Germany
[d] Ruhr-Universität Bochum, Inorganic Chemistry, 44801, Bochum, Germany
[e] Fraunhofer UMSICHT, Department of Electrosynthesis, 46047, Oberhausen, Germany
[f] RWTH Aachen University, Electrochemical Reaction Engineering (AVT.ERT), 52074, Aachen, Germany
[g] JARA-ENERGY, 52056, Aachen, Germany

ARTICLE INFO

Keywords:
Green hydrogen
Wind power
Renewable energy sources
Water electrolysis
Dynamic operation
Degradation analysis

ABSTRACT

The direct coupling of wind turbines to water electrolyzers promises scalable, green hydrogen production, but little is known about the impact of the fluctuating power provided by renewable energy sources on electrolyzer longevity. Therefore, we developed a realistic, semi-synthetic wind power profile to operate polymer electrolyte membrane (PEM) and alkaline water electrolysis (AWE) cells. We also established two analysis methods for the dynamically obtained I-V data. The methods enable the extraction of I-V curves, voltage degradation, and resistances. A major advantage of these methods is the highly accurate extraction of performance metrics without interrupting dynamic operation. Cell voltage degradation in both electrolysis technologies depends on both the current density and operation mode. While extracting an accurate ohmic cell resistance for AWE cells proved challenging, we found good agreement for PEMWE cells with the high-frequency resistance measured by impedance spectroscopy. With the proposed methods, the stability of all types of electrolysis systems can be studied during dynamic operation.

1. Introduction

Hydrogen is considered a promising sustainable energy carrier, if produced using renewable energy sources. Currently, hydrogen is mostly generated via the steam reforming of natural gases, with less than 4 % of production utilizing electrolysis [1]. Water electrolysis powered by wind and solar power is currently the most likely scalable source of sustainable hydrogen [2–4]. In order to achieve independence from fossil fuels and reduce harmful greenhouse gas emissions, the share of hydrogen produced with electricity from solar and wind power plants must be significantly increased. As solar and wind power plants are highly dynamic energy sources, the continuous recording and evaluation of performance data without interrupting the dynamic operation of electrolysis stacks is essential for the early detection of aging or potential failures. This is especially important, as the influence of dynamic operation on electrolysis systems is largely unknown [5,6]. Previous efforts to evaluate water electrolyzers with highly dynamic power supplies have interrupted their operation to record I-V curves or impedance spectra [6–8]. These techniques are essential for analytical purposes, but for electrolyzers in application, the recording of polarization curves is not practicable, as operation must be interrupted and the available power from renewable energy sources cannot be used optimally. To date, no reports have been published on cell voltage changes during the uninterrupted dynamic operation of alkaline water electrolysis (AWE) and polymer electrolyte membrane water electrolysis (PEMWE) cells. To address this research gap, we developed a realistic wind power profile and two analysis methods for extracting I-V curves, ohmic cell resistances, and voltage degradation rates from wind profile operation of AWE and PEMWE cells. We validated the results by comparing them with conventional measurement methods like I-V curves and high-frequency impedance and demonstrate extraction

* Corresponding authors.
E-mail addresses: s.zerressen@fz-juelich.de (S. Zerressen), a.gluesen@fz-juelich.de (A. Glüsen).
[1] Authors contributed equally.

https://doi.org/10.1016/j.ijhydene.2025.03.387
Received 18 December 2024; Received in revised form 6 March 2025; Accepted 28 March 2025
Available online 11 April 2025
0360-3199/© 2025 The Authors. Published by Elsevier Ltd on behalf of Hydrogen Energy Publications LLC. This is an open access article under the CC BY license (http://creativecommons.org/licenses/by/4.0/).

from uninterrupted operation for up to 447 h. In the following, we refer to properties obtained through the analysis methods as *extracted* and those obtained through conventional recording methods as *recorded*. Additionally, until now, degradation of AWE and PEMWE have only been studied separately. Here, we show degradation of both systems under the same conditions.

1.1. Dynamic operation of alkaline water electrolysis cells

AWE constitutes a fundamental and mature technology for large-scale electrochemical hydrogen production [9,10]. Originally, AWEs were engineered for steady-state operation under fixed process conditions [5]. On the contrary, renewable energy sources are highly dynamic and intermittent. Compatibility with highly dynamic power input is complicated by the partial load limits that are imposed for safety reasons [9]. With a low partial load, the diffusive hydrogen flow across the separator remains constant, whereas low current densities reduce the amount of oxygen produced. This means that explosive gases can be formed. However, recent advances in process design are able to reduce the gas impurities [11]. Another important factor for the viability of AWE under dynamically changing conditions is long-term stability. In AWE, data regarding long-term stability are limited and practically non-existent for dynamic operation [12,13]. For stationary operation, degradation rates in the range of $0.4\,\mu V\,h^{-1}$ to $600\,\mu V\,h^{-1}$ have been reported [14,15]. In contrast, only few researchers have reported long-term stable operation using renewable energies, and no determination and analysis of aging rates has yet been carried out [16–19]. Nevertheless, the ability of the system to respond to dynamic changes has been found to be high. In general, extended operation at high current densities, prolonged periods of open circuit voltage (OCV), frequent temperature fluctuations, and recurrent load changes within a system can accelerate degradation processes [12]. Considering the various phenomena in AWE, it is important to investigate aging rates, especially under dynamic conditions.

1.2. Dynamic operation of PEM water electrolysis cells

Polymer electrolyte membrane (PEM) electrolyzers are well adapted to dynamic operation, making this technology a good match for highly dynamic power sources [20–25]. Under highly dynamic power input, similar to AWE, repeated switching to OCV leads to the accelerated degradation of PEM electrolyzers [8,26]. When switching 3000 times to OCV within 1000 h of operation, Weiß et al. [27] observed a higher degradation rate of $50\,\mu V\,h^{-1}$ vs. $16\,\mu V\,h^{-1}$ when switching only 80 times to OCV over the same time span. Additionally, high rates of change during operation lead to higher degradation than lower rates, e.g., near instantaneous change in a rectangular profile versus a constant rate of change in a triangular one of the same periodicity. These impacts are the most pronounced for PEMWEs with low anode catalyst loading [6], implying that the catalyst layer is more affected by dynamism than every other component of a PEMWE. A performance increase during dynamic operation between $0\,A\,cm^{-2}$ and $2\,A\,cm^{-2}$, demonstrated by Frensch et al. [8], was attributed to membrane-thinning which could be caused by radical formation during idle periods due to gas crossover. However, membrane-thinning is not desirable, as it could lead to an early failure of the membrane. If periods of OCV, sudden changes between high and low current densities or cell voltages are avoided, dynamic operation can benefit the lifetime of PEM water electrolyzers [6–8]. Furthermore, interruptions can distort the representation of performance in dynamic operation. Consequently, the dynamic performance of electrolyzers is better reflected by extracting performance data from dynamically recorded data.

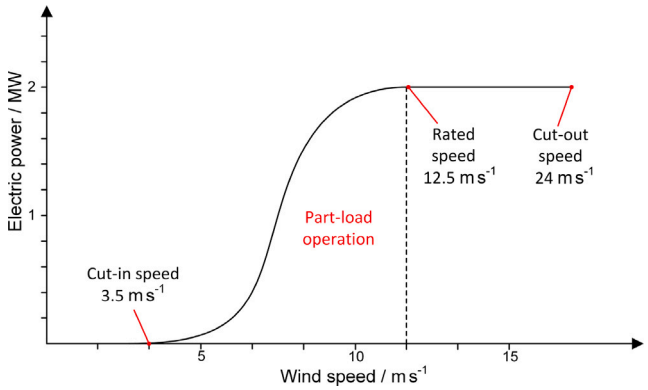

Fig. 1. Dependency of the electric output power of a 2 MW wind turbine on wind speed [31].

2. Methods

2.1. Wind power profiles – semi-synthetic potential and current profiles

The wind load profiles within this work were generated from measured wind speed data, which were provided by the HTW Berlin [28]. These data comprise wind speed information recorded at an interval of 1 s and measured at a weather station on the roof of the HTW Berlin building with a height of approximately 25 m. To depict a specific application scenario for the wind load profiles of electrolyzers, a medium-sized wind turbine model with a nominal output of 2 MW (Vestas V90-2MW) [29–31] was chosen. The following steps are necessary to convert the wind speed data into a power profile of the wind turbine for subsequent use for the electrolyzers. First, the measured wind speed needs to be converted into wind speed at hub height of the wind turbine. The selected 2 MW wind turbine features a hub height of $h = 80$ m. The characteristics of the terrain at the turbine's location also significantly influence wind conditions and therefore must be considered. According to [30], Eq. (1) represents the wind speed at hub height v_{hub} ($m\,s^{-1}$) depending on the measured wind speed v_{25} ($m\,s^{-1}$) at 25 m and the existing terrain.

$$v_{hub} = v_{25}\left(\frac{h}{25}\right)^{g} \tag{1}$$

The value for parameter g with a magnitude of 0.4 characterizes the terrain of a city center and is given by Anjum et al. [32]. The resulting power generated by the wind speed v_{hub} can be derived from the kinetic energy of the air mass flow. With the power coefficient C_p of the 2 MW wind turbine [29], Eq. (2) expresses the generated power $P_{turbine}$, according to [31],

$$P_{turbine} = C_p\frac{1}{2}\rho\pi r^2 v_{hub}^3 \tag{2}$$

where $\rho = 1.225\,kg\,m^{-3}$ is the density of air at atmospheric pressure and $r = 45$ m the radius of the rotor blade. Depending on the power coefficient C_p of the wind turbine, the generated power $P_{turbine}$ is limited to a rated wind speed of $13\,m\,s^{-1}$ to reduce mechanical loads and also needs a cut-in wind speed of $4\,m\,s^{-1}$ to start working [30,31]. To generate a highly dynamic power profile, the wind turbine must primarily operate in the so-called part-load range, which lies between the cut-in and rated wind speed. Operating in full-load range with a wind speed higher than $13\,m\,s^{-1}$ would result in a power profile with little dynamics, as the pitch control of the wind turbine keeps the extracted power from wind energy constant. Fig. 1 depicts this relationship between power output and wind speed for the 2 MW wind turbine. With the adapted wind speed from Eq. (1), a wind speed profile depicting wind speeds for 8.33 h on a gusty day in February was utilized to obtain a highly dynamic profile.

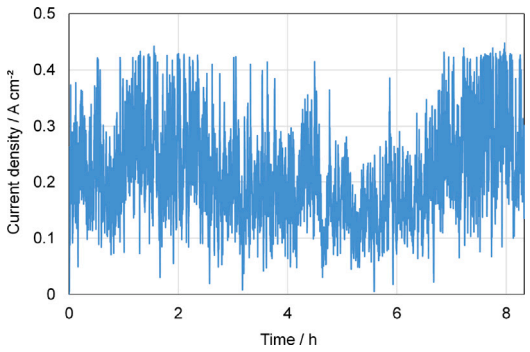

Fig. 2. Galvanodynamic wind profile for AWE.

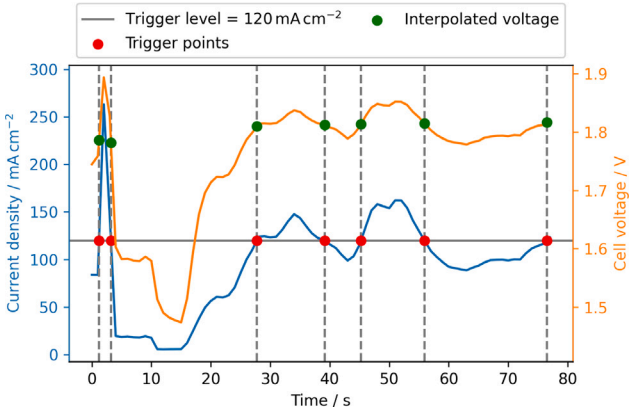

Fig. 3. Graphical representation of the trigger method: the current density (blue) crosses a selected trigger level (gray). By using linear interpolation to first estimate the crossing (red circles), we subsequently find the crossing time (vertical dashed lines) and from that the coincident cell voltage (green circles). (For interpretation of the references to color in this figure legend, the reader is referred to the web version of this article.)

To realistically simulate the dynamics of the profile, the inertia of the wind turbine is also considered. Therefore, the inertia constant, H of a 2 MW wind turbine, is introduced with a quantity of 3 s [33]. H represents the time in which the wind turbine can maintain its rated power with the energy stored in the rotation masses. To reflect the inertia of wind on the power output, a first-order low-pass filter was integrated into the calculation. With the Laplace transform, Eq. (3) shows this correlation, wherein s is the complex-valued parameter of the Laplace transform, the electric power results:

$$P_{el} = \frac{P_{turbine}}{1 + 2Hs} \tag{3}$$

To utilize the generated 2 MW wind profile for AWE and PEMWE at a laboratory scale, a linear down scaling to the respective power class of the individual cells must be performed. The nominal power of the single electrolysis cells is 4 W for AWE and 80 W for PEMWE. These values were used to adjust the electric output power P_{el} for individual single electrolysis cells. The adaptation considered the specific power characteristics of each technology to ensure a realistic scaling of energy conversion. To clarify the linear relationship, the electric output power was scaled proportionally to the nominal power of each electrolysis cell, as illustrated in Figure S1, Supporting Information for AWE and Figure S2, Supporting Information for PEMWE. The adapted power was then converted into cell voltage or current profiles using the I-V characteristics of the respective electrolysis cells. This conversion enabled the generation of potentiodynamic and galvanodynamic wind load profiles for testing. Fig. 2 provides an example of a wind load profile derived from the measured wind speed data, further illustrating the methodology used in establishing the linear relationship.

2.2. Data analysis

We developed two methods to extract I-V curves from and track cell voltage changes and ohmic resistances during measurements of water electrolyzers under highly dynamic power supply: a trigger based method and a surface fit one. Both analysis scripts are written in Python and rely on SciPy [34] for least squares curve fitting. All illustrations in this section are based on a measurement of an alkaline water electrolysis cell. These data contain multiple repetitions of the 8.33 h wind profile, which is necessary to prevent the specific properties of the profile from biasing the extracted voltage degradation.

For the trigger method (Fig. 3), we select a range of current levels at which we would like to sample the corresponding cell voltages. We chose these levels by dividing the range from minimum to maximum current in the measurement by six. We discarded the maximum and minimum and then rounded to the next convenient decimal to obtain four levels, which are well distributed within the measured range (e.g. 50 mA cm^{-2}, 100 mA cm^{-2}, 200 mA cm^{-2}, 300 mA cm^{-2} for the AWE measurements, see Fig. 4). To extract more detail, more levels can be chosen in exchange for additional computations. When examining one of the selected current levels, we find that in general none of the measured currents exactly match the selected current level. Therefore, for each selected current level our method finds the points before and after this trigger current level was crossed. The program then interpolates linearly between these points to find an estimate for the true crossing time. The algorithm linearly interpolates between the simultaneous voltage measurements to find an estimate for the time-coincident cell voltage.

This time-coincident voltage is a good performance indicator if the voltage follows current changes closely at the highest expected current change rates. A frequency analysis of the wind profile we use shows 80 % of the energy being generated at or below 0.08 Hz. The slowest sampling time at one of our test stands is 5 s and, therefore, still sufficient to properly resolve such frequencies (Nyquist frequency of 0.1 Hz), whereas the profile is sampled even faster (1 s). Impedance spectroscopy of our cells indicates negligible current–voltage phase delay at 0.08 Hz, i.e. electrical properties of the cell also do not impact time coincidence significantly. These prerequisites apply to both methods shown here. In addition, the fast sampling compared to the profile dynamics makes linear interpolation the most appropriate choice for the trigger method as little accuracy is gained from higher order methods while linear interpolation keeps computational load low and avoids overshoots and similar artifacts of other methods.

The repetition of this process for all crossings yields one point cloud per trigger level (Fig. 4). To each cloud, we fit a linear function whose slope gives the aging rate in terms of voltage changes. To check the method's plausibility, we interrupted the dynamic measurement to record I-V curves and compare them to the extracted curves (Figure S3, Supporting Information). After each interruption, the cell voltage drops for less than 8 h before the vanishes in the noise floor again (Figure S4 and S12, Supporting Information). We discard data from these time periods to avoid biasing the fit toward lower cell voltages.

As an alternative to the trigger method we developed a method based on directly fitting a model to the wind profile data. This is illustrated in Fig. 5. For every measurement three values are available, namely time, current density, and cell voltage. The data can be represented as a point cloud in three-dimensional space (Fig. 5(a)). The cloud is resembling a bent sheet, curving downwards toward lower values of the current density axis. This shape can be described by a simple, well-established model of the I-V curve, that combines Ohm's law and the Tafel equation [35–37]. As we expect the I-V characteristic to change over the course of the experiment, we extend the model by making its

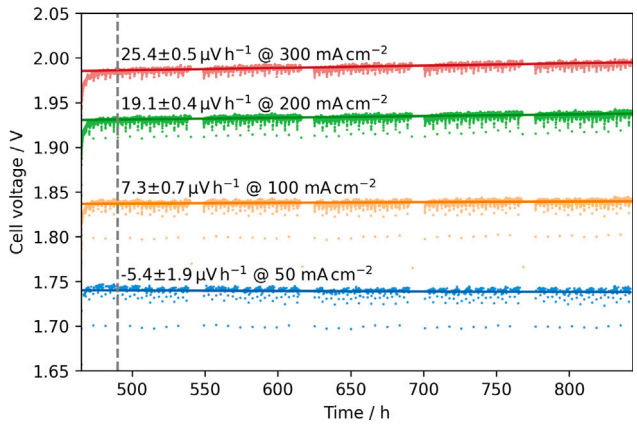

Fig. 4. Coincident voltages at four fixed trigger currents and corresponding linear fits (start marked by dashed vertical line). Some points have been excluded from the fit: the re-start (465 h to 490 h) after concluding uninterrupted operation and 8 h after each interruption of the dynamic operation.

parameters time-dependent:

$$U(j,t) = r(t)j(t) + b(t)\log\left(\frac{j(t)}{j_{\mathrm{ref}}}\right) + n(t) \tag{4}$$

Where $U(j,t)$ is the current density dependent cell voltage, $r(t)$ the area-specific resistance, $b(t)$ the Tafel slope, j_{ref} the reference current density (1 mA cm^{-2} here). The reference current density ensures a unitless argument of the logarithm. The j-independent parameter $n(t)$ parameter contains the exchange current density j_0 in the form of $\log\left(\frac{j_{\mathrm{ref}}}{j_0}\right)$, the reversible cell voltage and any other voltage offsets. In turn, the fit provides an estimate of $r(t)$, $b(t)$, $n(t)$ and allows for assigning the degradation to one or more of these parameters. In contrast to validation values from impedance spectra (Sections 4.2.3 and 5.2.3), r is not associated with a specific current density. Evaluating the model at a fixed time gives an extracted I-V curve. Within the margins of error of our measurements, the two curves agree at low current densities, while the extracted curve shows a higher voltage otherwise. The root mean square error is 29.7 mV, see Fig. 5(b).

We model the time-dependency of $r(t)$, $b(t)$, and $n(t)$ using piecewise linear functions. Such functions are collections of linear functions continuously chained together at predefined time axis values. The pieces begin and end exactly when the dynamic operation was interrupted or the measurement began or ended, for the example presented here at 465 h, 475 h, 485 h, 540.9 h, 616.7 h, 692.6 h, and 843.5 h. Without interruptions, these points can be chosen freely. Fig. 5 exemplifies the flexibility afforded by the piecewise linear functions by fitting the re-start phase (465 h to 490 h) at the beginning and by allowing us to extract I-V curves even within gaps left by interruptions. When extracting I-V curves, we evaluate the fitted function (the surface) at a fixed time (extraction time) and for a range of current values from the minimum to the maximum we measured during dynamic operation. We call this operation "slicing". For context we also add data from 12 h before and after the evaluation time as points. From how well the extracted I-V curve matches the point cloud we can infer how well the surface fit represents the I-V characteristic of the cell during the part of the experiment around the extraction time (see Figure S10). Just like with the trigger method, we want to evaluate the overall trend and therefore exclude data 8 h after each interruption. The average aging rate over a given time is calculated by averaging the slopes of the pieces weighted with their respective lengths.

The residuals of the surface fit and trigger methods are approximately normally distributed which shows that the model is not missing a systematic trend in the data, which would lead to a skewed histogram or even multiple peaks. We found standard deviations of 2.8 mV (AWE) and 1.4 mV (PEM) for the surface fit, as well as 1.7 mV to 3.5 mV (AWE) and 2.7 mV to 11.0 mV (PEM) for the trigger method. These standard deviations are in a range that can reasonably be explained by measurement errors introduced by the potentiostat via current inaccuracies. Because the surface fit includes all data, except those 8 h after each interruption, and does not rely on interpolation, we are more confident in its results and extract I-V curves and resistances with this method in the following. In addition, only the surface fit method provides satisfactory estimates of model parameters such as $r(t)$. However, due to lower computational load, the trigger level method is better suited for an online implementation. It also does not rely on a model of the current voltage relation, which makes the method useful in situations where this relation is unknown, such as in the case of mass transport limitations.

3. Experimental

3.1. Alkaline water electrolysis

3.1.1. Electrolysis cell and test bench

An in-house-designed alkaline electrolysis single cell and in-house-developed test rig, as previously described by Karacan et al. [38], was used. Industrial nickel expanded metal on the anode side and nickel woven mesh on the cathode side were used as electrodes (nickel purity > 98 %). The size of the electrodes was 5 cm^2. To ensure a low and constant contact resistance, the electrodes were welded into a nickel frame (Figure S5, Supporting Information). As the woven mesh can only be welded onto the frame and not into the frame, the electrode is sealed to the outside with a polytetrafluoroethylene (PTFE) gasket. The frames also serve as current collectors. Zirfon™ Perl UTP 220 (Agfa-Geveart N.V.) was used as the separator with a size of 4.6 cm×4.6 cm. The separator was sealed to the outside with a 200 µm-thick PTFE sealing. The liquid electrolyte used was an aqueous potassium hydroxide (KOH) solution with 30 wt % KOH (Merck, pellets for analysis EMSURE® ≥85 %). The density of the solution was determined using a density meter (Anton Paar DMA™ 35) and the electrolyte concentration was calculated from the density and temperature of the electrolyte [39]. The liquid anolytic and catholytic electrolyte cycles were connected by an equalization line. For a constant process concentration, the electrolyte level was kept constant and ultrapure water was regularly dosed using a liquid level sensor. To minimize the influence of metallic impurities on the cell's performance, the electrolyte is not in contact with metallic components. However, impurities in the electrolyte itself cannot be completely ruled out [40,41]. The electrolyte was pumped through the electrolysis cell by two membrane pumps (KNF SIMDOS® 10 FEM 1.10 RC-P) with a flow rate of 30.0 ± 0.6 mL min^{-1} to the electrolysis cells from the electrolyte containers. In order to maintain a constant process temperature, the flow fields were constantly heated to 80 ± 1 °C by two heating rods in the flow fields. The temperature was controlled and limited by the process control of two sensors (Unitherm, 1KI15 ML-100 sheathed thermocouple) in the flow fields. A potentiostat (BioLogic BCS-815 battery cycler) was connected to apply voltage or current.

3.1.2. Electrochemical test protocol

The cells were initially started with a current density step of 20 mA cm^{-2} for 20 min. The galvanodynamic wind profile, as described above, was then applied. The described 8.33 h profile was repeated up to a total duration of 465 h in a galvanodynamic mode with a current density range from 5.3 mA cm^{-2} to 447.5 mA cm^{-2}. The selected current density range was determined in a preliminary experiment to correspond to a voltage range of 1.45 V to 2 V, aligning with the voltage range chosen for the PEMWE system. As described below, a galvanodynamic operation is more suitable in this context than a potentiodynamic approach. Operation was then interrupted for a few seconds and the same galvanodynamic profile with interruptions by I-V curves and impedance spectra every 75 h was carried out. This time interval is based on literature and has additionally been determined in

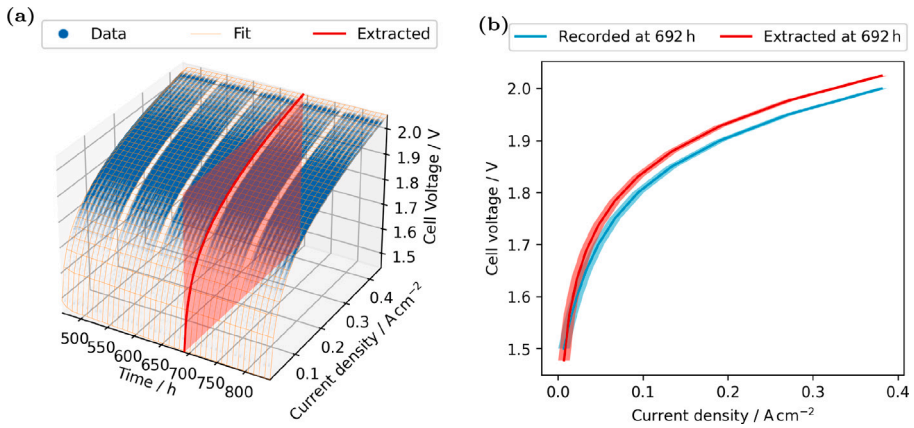

Fig. 5. a: 3D data point cloud, surface fit as wireframe and extracted I-V curve with cross-sectional plane. Gaps in the point cloud are caused by the exclusion of data 8 h after each interruption. b: Extracted I-V curve and recorded curve, both at 691.8 h. The shaded area around both curves shows the respective measurement error margins. The root mean square error (RMSE) between them is 29.7 mV.

preliminary testing [6]. It has proven to be sufficient to stabilize the system after an interruption and to ensure that the voltage returns to the value observed before the interruption. Current, cell voltage and cell temperature were recorded every second. Galvanostatic polarization curves were recorded to compare the performance using conventional methods and the polarization curve extracted from dynamic operating data. I-V curves were taken between 1.5 V and 2.0 V with 50 mV steps. Each step was held for 3 min. The I-V curves were generated from the average current of the last minute at each step. Impedance spectra were recorded to compare the extracted ohmic cell resistance from the surface fit with the recorded ohmic resistance. The impedance spectra were recorded immediately after the I-V curve. The spectra were recorded at 1.5 V in a frequency range from 10 kHz to 1 Hz and an amplitude of 20 mV. High frequency resistances were derived by means of the equivalent circuit approach using the ZView® software. The equivalent circuit consisted of one series inductive element, one series resistance, and two constant phase element (CPE)-resistance parallel elements. This approach allows for the separation of ohmic losses and polarization losses, while the high-frequency resistance accounts for both electrical and ionic contributions [42]. The equivalent circuit model is shown in S11. The ohmic resistance was determined from the intersection of the fit with the real axis of the derived Nyquist plot.

3.2. Polymer electrolyte water electrolysis

3.2.1. Electrolysis cell and test bench

For PEMWE single cell tests, an in-house-build test rig, developed and built by Rakousky [35], was used, in which five PEMWE cells can be run simultaneously. Each cell is equipped with its own current circuit, voltage measurement, temperature control and measurement, heating rods and water supply for the anode and cathode sides. One peristaltic pump delivers water separately for the anode and cathode circuits. The water flow rates were $25.0 \pm 1.5\,mL\,min^{-1}$ on the anode and $24.0 \pm 2.5\,mL\,min^{-1}$ on the cathode sides. The deviation between these flow rates may be due to different compression of the tubes by the roller cassette. The water was purified to a conductivity of $0.055\,\mu S\,cm^{-2}$ and a total organic carbon (TOC) content of less than 3 ppb and was heated via glass heat exchangers for a water input temperature of 80.0 ± 1.6 °C. The cell temperature of the end plates was measured with two NiCr-Ni thermocouples and controlled at 80 ± 1 °C from an in-house built temperature control. Ion exchangers were installed between the water storage tank and the cell inlet to ensure that no impurities entered the cells. A TDK Lambda GEN-20-76 DC power supply was used as the power supply and the cell voltages were recorded using a Keithley model 2701 multimeter. The power supplies were controlled via LabVIEW-based software. The steps of the changes of the operating point in the wind profile were 1 s, whereas the sample rate was 5 s during the dynamic measurements and the recording of the I-V curves.

Like the test bench, the PEMWE cells are in-house-built. The anode and cathode monopolar plates are made of titanium and coated with platinum and gold, respectively. The end plates include a serpentine flowfield to transport water over the active cell area of 17.64 cm^2. Commercially available titanium felts from Bekaert with a thickness of $363 \pm 8\,\mu m$, an average porosity of 68 % and an average fiber diameter of 20 µm were used as the anode porous transport layer (PTL) and sealed with PTFE gaskets with the same thickness. For the cathode side, carbon paper with a thickness of $367 \pm 1\,\mu m$ from Toray (TGP-H 120 Toray®) was utilized. The thickness of the gasket was chosen to realize a cathode PTL compression of 29 %. All titanium PTLs were cleaned in an ultrasonic bath in propan-2-ol and water. To avoid titanium oxidation during electrolysis operation, all titanium PTLs were coated with 150 nm platinum by SYSTEC Vacuum Coating GmbH & CO KG from one side. Additionally, the back sides of the PTLs were sputtered at IET-4 with platinum in a sputter coater from Quorum (Q150T) at 30 mA and 0.7 Pa under Argon. The sputter time was 360 s and the loading $0.060 \pm 0.008\ mg_{Pt}cm^{-2}$. Catalyst coated membranes (CCMs) were manufactured in-house by means of the decal method. For the anode catalyst layers, dispersions of IrO_2 (Alfa Aesar, Premion, 99.99 % metal basis, Ir 84.5 % min) in heptanol with a 10 wt% water-based Nafion™ dispersion from Ion Power were prepared, homogenized in an ultrasonic homogenizer (Bandelin Sonoplus) for 300 s, coated onto an PTFE coated inert decal transfer foil with a doctor blade coater (Coatmaster 509 MCI, Erichsen GmbH & Co. KG), and dried at 60 °C for 3 h. The solid contents of Nafion™ in the anode catalyst layers were 25 wt%. For the cathode catalyst layers, 60 % Pt/C (HiSPEC 9100, Johnson & Matthey) was mixed with a 15 wt% alcohol-based Nafion™ dispersion from Ion Power, butanol and ethylene glycol, and also doctor blade coated. The solid contents of Nafion™ in the cathode catalyst layers were 20 wt%. The dried electrodes were hot-pressed onto Nafion™ 117 from Chemours at 130 °C. The resulting loadings were $1.00 \pm 0.12\ mg_{Ir}cm^{-2}$ (standardized to Ir metal) for the anode catalyst layers and $0.23 \pm 0.03\ mg_{Pt}cm^{-2}$ for the cathode catalyst ones.

3.2.2. Electrochemical test protocol

First, the cells were heated up to 80 °C for 1 h. This was followed by a conditioning phase in which the cells were ramped up from 1.5 V to 1.7 V in 0.5 V-steps every minute and then operated for 15 h at 1.7 V, following the conditioning process proposed by [43]. Afterwards, two I-V curves and nine impedance spectra were recorded between 1.45 V to 2 V. The cells were then operated for 350 h with the repeated 8.33 h potentiodynamic wind profile scaled to the power of a representative

PEM cell (Figure S2, Supporting Information), as described in Section 2 with cell voltage limits between 1.45 V to 2 V. The potentiodynamic wind profile is displayed in Figure S8, Supporting Information. After 350 h, the third I-V curve was recorded followed by the same impedance protocol as applied before the dynamic operation. From then on, an I-V curve was recorded after nine wind profile repetitions (75 h) and the cells were operated for a further 611 h. Current, cell voltage and cell temperature were recorded every 5 s. Recorded I-V curves for comparison with I-V curves extracted from dynamic data were recorded potentiostatically in 50 mV steps from 1.3 V to 2 V and additionally two steps at 1.48 V and 1.53 V (20 mV to 30 mV steps) in the activation region. Each voltage step was held for 5 min. The I-V curves were then generated from the mean values of the last 10 measuring points (50 s) of a voltage step. Impedance spectra were recorded potentiostatically at 1.45 V, 1.5 V, 1.55 V, 1.6 V, 1.65 V, 1.7 V, 1.8 V, 1.9 V and 2 V with a Biologic HCP 1005 potentiostat in a frequency range between 100 mHz and 10 kHz and an amplitude of 5 mV. High-frequency resistances, which represent the ohmic cell resistance, were derived from equivalent circuit fitting using the software ZView®. The equivalent circuit consisted of an inductance in series with an ohmic resistance and two resistances in parallel with constant phase elements (LR(RQ)(RQ), see Figure S11).

3.3. Potential- and current-controlled dynamic operating profiles

When coupling an electrolyzer with a renewable energy source, it should ideally follow the generated power profile. However, as test benches cannot control power as an input signal, potential or current-controlled profiles must be used. Both approaches can be found in the literature. The harmonized EU protocol for low-temperature water electrolysis testing assumes current-controlled operation, which is common in industrial applications [44]. A challenge of current-controlled operation is that the potential can shift beyond desired ranges, leading to shutdowns or potentially accelerated aging. Although current and voltage are related, the potential is considered the driving force of aging phenomena [45]. In voltage-controlled measurements, capacitive currents can cause over- or undershoots [46]. They can occur when the voltage changes and the electrochemical double layers are first charged or discharged. Then exclusively capacitive current flows and only when the set voltage is reached, the current becomes faradaic again. These capacitive currents can distort measurement data, making subsequent analysis more challenging. Whereas filtering out negative current values resulting from capacitive undershoots is feasible, any positive values resulting from over- or undershoots are difficult to remove. Extensive filtering is required to remove values within the capacitive current period. In such cases, a current-controlled measurement can avoid data distortion. Although the voltage lags behind the current, the distortion is less pronounced. As there was large distortion in the alkaline measurements when using a potentiodynamic wind profile, the galvanodynamic profile described above was used. The comparative results of current-controlled and voltage-controlled profiles for AWE can be found in the Supplementary Information (Figure S6). As the recording of the current and voltage worked differently for the PEMWE cells than for the AWE ones, it was possible to operate the PEMWE cells with a potentiodynamic wind profile without recording capacitive over- or undershoots in the current. Therefore, both current-controlled measurements of AWE cells and potential-controlled measurements of PEMWE cells are evaluated in the following. Thus, we were able to test our methods with galvanodynamically and potentiodynamically recorded data.

4. Results and discussion of alkaline water electrolysis

4.1. Trigger level method – Temporal performance tracking of cell voltage changes

To analyze the temporal development of the cell voltage using the trigger level method, the data of the applied wind profile over a total duration of 843 h was used. The first 488 h ran without interruptions.

As seen in Fig. 6(a), in the beginning of the measurement, a deactivation phase of the cell is observed – the cell voltage is initially low and increases exponentially. This phase lasts approximately 200 h and could be attributed to the absorption of hydrogen into the metal lattice on the cathode, leading to the formation of a β-nickel hydride phase [47–52]. Due to the change in the d-band during hydride formation, the activity toward the hydrogen evolution reaction (HER) decreases, resulting in a loss of electrocatalytic activity. Huot and Brossard [47] describe deactivation initially occuring due to hydrogen absorption and nickel hydride (NiH_x) formation, followed by deactivation due to metallic impurities in the electrolyte. Additionally, iron can lead to activation or deactivation, depending on the amount in the electrolyte [40,41]. Overall, the deactivation seen in our experiments was about 150 mV. A small data gap is observed at around 350 h, resulting from a brief interruption in recording, whereas the wind profile continued during this time. In the shown example, aging rates for current densities of 50 mA cm^{-2}, 100 mA cm^{-2}, 200 mA cm^{-2}, and 300 mA cm^{-2} were examined. The lowest current density exhibited an aging rate of $9.3 \pm 3.0\,\mu V\,h^{-1}$. Higher current densities exhibit aging rates ranging from $31.2 \pm 1.2\,\mu V\,h^{-1}$ to $57.8 \pm 0.8\,\mu V\,h^{-1}$. The observed aging rates of fall within the range of reported degradation rates for stationary AWE operation ($0.4\,\mu V\,h^{-1}$ to $600\,\mu V\,h^{-1}$) [14,15]. Given the limited availability of long-term stability data for dynamic operation, these results provide valuable insights into the performance of AWE under dynamic conditions. When considering the measurements with interruptions (Fig. 6(b)), it is initially noticeable that there is a significantly shorter deactivation phase compared to the measurement without interruptions. This is because the second section of the experiment was carried out after only a short interruption of a few minutes following the previous section and the cell is already conditioned. Due to the resulting short deactivation phase, the first 10 h of data were excluded from the fit. This exclusion period ensures that the stabilization phase following a short interruption is omitted, allowing for a fit of the aging rate. As described in Section 2, the stabilization time for alkaline electrolysis is 8 h. With each interruption of the measurement by an I-V curve and impedance measurement, the voltage temporarily drops, followed by a brief deactivation. Therefore, the subsequent 8 h following each interruption were excluded so as not to distort the fit (see Figure S7, Supporting Information for a plot showing the interruptions). This observation aligns with expectations, given the brief interruption in measurement. Observations from previous studies thus suggest that the brief interruption and lower potentials for recording the I-V curve lead to a recovery of the anode and cathode and could thus lead to a subsequent reduction in cell potential. As indicated by various researchers, long-term cathodic and anodic effects leading to overpotential can be reversed through short interruptions, cycling, or applying low voltages, resulting in a “rejuvenation” of the electrode [18,49,53–57]. The resulting aging rates appear slightly lower, i.e., $-5.5 \pm 1.9\,\mu V\,h^{-1}$ for the lowest current density of 50 mA cm^{-2}, then increasing from $7.3 \pm 0.7\,\mu V\,h^{-1}$ to $25.4 \pm 0.5\,\mu V\,h^{-1}$ for current densities between 100 mA cm^{-2} and 300 mA cm^{-2}.

Thus, when comparing the measurements sections with and without interruptions, it is notable that the aging rates are lower for measurements with interruptions than without interruptions. We assume two potential explanations for the observed phenomenon. Firstly, it is plausible that the aging rate decreases over time. As the measurements with interruptions were conducted after those without interruptions, it is possible that the overall aging rate diminished. Another possibility is that this observation may suggest that interruptions, at least in the given single-cell setup, could positively influence the aging rate. The possibility of interruptions leading to a reduced overall cell voltage has also been described without further analysis in the literature [44].

4.2. Surface fit method

For the application of the surface fit method, we used the same uninterrupted and interrupted experimental wind data from AWE single cell tests as for the trigger method.

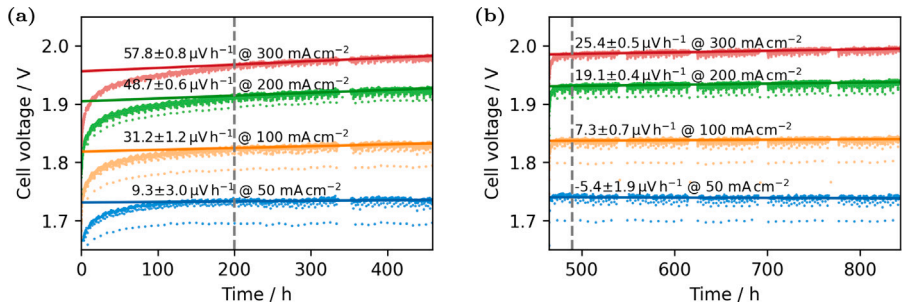

Fig. 6. Development of the cell voltage over time extracted for four selected current density levels using the trigger level method for alkaline water electrolysis cells, with an indication of the average voltage change for a: uninterrupted and b: interrupted cell operation. The vertical gray line represents the start of the fit.

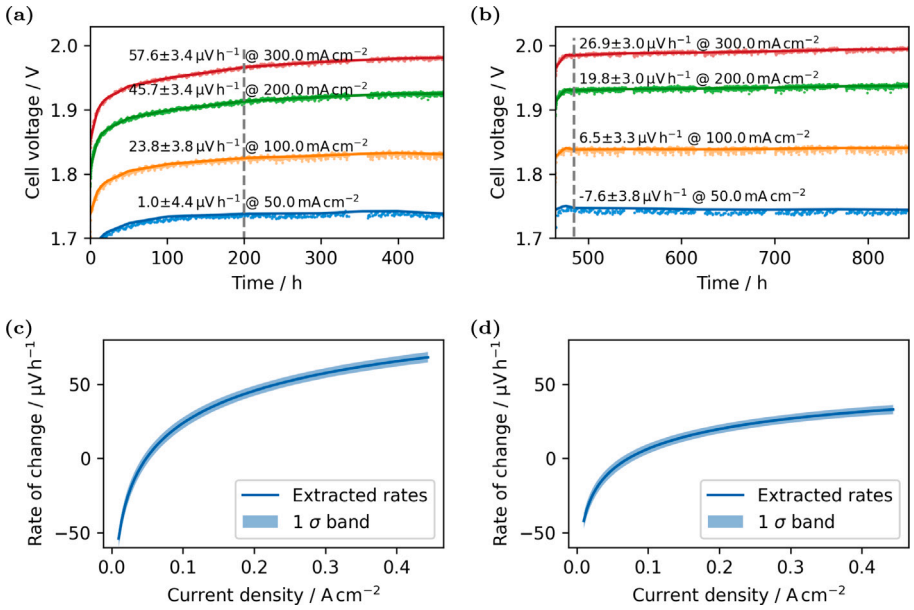

Fig. 7. Development of the AWE single cell voltage over time for four selected current density levels extracted using the surface fit method, with indication of a: the average voltage change for uninterrupted and b: interrupted operation, c: the rate of change of the voltage (slope) over the entire current density range for uninterrupted and d: interrupted operation.

4.2.1. Temporal performance tracking of cell voltage changes

The development of the cell voltage over time derived from the surface fit method is illustrated in Fig. 7(a)–(b) for the same current density levels of 50 mA cm^{-2}, 100 mA cm^{-2}, 200 mA cm^{-2} and 300 mA cm^{-2}. In the graphs, a small range of the measurement data around the surface fit is depicted. Again, the first 200 h and the subsequent data of 8 h following each interruption are excluded, as described above. For uninterrupted operation (Fig. 7(a)), slopes are in the range from $1.0 \pm 4.4\,\mu V\,h^{-1}$ to $57.6 \pm 3.4\,\mu V\,h^{-1}$. In fact, there is a zero crossing at approximately 44.5 mA cm^{-2} (Fig. 7(c)). For interrupted operation, the slopes for the chosen current density levels range from $-7.6 \pm 3.8\,\mu V\,h^{-1}$ to $26.9 \pm 3.0\,\mu V\,h^{-1}$ (Fig. 7(b)). Fig. 7(c)–(d) depict the resulting voltage slopes over the current density range. For interrupted operation, there is a zero crossing at approximately 97 mA cm^{-2} (Fig. 7(d)). This signifies that lower current density levels tend to exhibit a reduction in voltage over time, whereas higher current densities show an increase in voltage over time. The changes observed in the upper and lower current density levels could be attributed to overlapping effects. In the lower current density range, activation overvoltages dominate. Conway et al. [56] propose that cyclic operation in the lower range might lead to the dissolution of NiH_x on the cathode, resulting in an improvement. Additionally, factors such as the adsorption of iron from electrolyte impurities could contribute to activation and enhancement [40]. It is also noteworthy that capacities may play a role in the lower current density range, potentially introducing some distortion to the fit as explained in 3.3 [46]. In the upper current density range, the overvoltage increases more strongly over time. This phenomenon could indicate an interplay of kinetic and ohmic effects. Ohmic effects could be attributed to the formation of oxides on the anode, leading to elevated contact resistances and active site blockages [55]. Additionally, factors such as bubble coverage and microbubble blockage may also play a role [37].

Reported degradation rates in the literature for experiments under constant process conditions range between $0.4\,\mu V\,h^{-1}$ to $600\,\mu V\,h^{-1}$ [14,15]. Thus, the recorded degradation rates in our study fall within the lower range reported in the literature. However, it is essential to note that the shown measurements were recorded dynamically, making a direct comparison with uninterrupted, stationary cells challenging. To evaluate the positive or negative impact of dynamic operation compared to stationary process conditions on aging, further direct comparative experiments are necessary.

Overall, the study demonstrates that the time-dependent cell voltage varies with the current density level.

4.2.2. Extraction of I-V curves

By slicing the surface fit of the wind profile, I-V curves can be extracted. This method enables a direct comparison between the extracted and recorded I-V curves at the same time, as further explained in Section 2.2. The results indicate a clear discrepancy between the extracted and recorded I-V curves, as illustrated in Fig. 5. Throughout

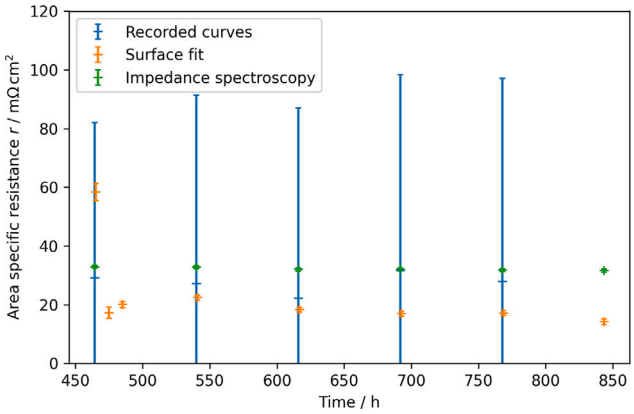

Fig. 8. Development of ohmic cell resistances of AWE from fit to the recorded curves (blue), fit to the surface plot (orange), and high-frequency resistances from EIS (green). (For interpretation of the references to color in this figure legend, the reader is referred to the web version of this article.)

the polarization range, the recorded I-V curve consistently lies below the extracted one, except in the range of very low current densities. In the presented example, the root mean square error (RMSE) between the curves is 29.7 mV. This trend, where the recorded curve exhibits a lower cell voltage than the extracted one, persists throughout the entire duration of the second section of the experiment with interruptions. As described above, a short interruption can lead to a "rejuvenation" of the electrodes, resulting in the improved recorded I-V curves after an interruption.

The results underscore that recorded I-V curves may not precisely align with the actual system performance. Employing a model and fitting enable the extraction of performance parameters during electrolysis operation, providing a more accurate representation of the system's behavior. The insights contribute to a nuanced understanding of electrolysis performance, emphasizing the significance of data extraction without interruption for a comprehensive assessment during dynamic operations.

4.2.3. Development of ohmic cell resistance

Using Eq. (4), the ohmic cell resistances could be determined for both the recorded and extracted I-V curves from the surface fit. In addition, electrochemical impedance spectra (EIS) were recorded during the interruptions to compare the resistances obtained from the fitting. The resistances from the fit to recorded curves are $22.2 \pm 4.2\,m\Omega\,cm^2$ to $31.7 \pm 4.4\,m\Omega\,cm^2$, from the surface fit $15.8 \pm 0.7\,m\Omega\,cm^2$ to $21.3 \pm 0.9\,m\Omega\,cm^2$, and $31.6\,m\Omega\,cm^2$ to $32.9 \pm 0.5\,m\Omega\,cm^2$ from EIS (see Fig. 8). The ionic resistance of Zirfon at 80 °C in 30 wt% was given as $50\,m\Omega\,cm^2$ [58]. It has been shown that the resistance in zero-gap electrolyzers can deviate from the resistance given in the data for Zirfon [37], and the resistances were measured in a range of $67\,m\Omega\,cm^2$ to $160\,m\Omega\,cm^2$ for UTP 220 [59,60]. The resistances reported in this study are slightly lower compared to the reported Zirfon data.

The discrepancy between the different resistances can stem from various reasons. On the one hand, more data is included in the surface fit using Eq. (4) than in the impedance measurements. Furthermore, the assumption of a constant Tafel slope in I-V fitting can result in variations of the resistances obtained from EIS and from the fitted values. Other possibilities for deviations could be different bubble behavior under stationary and dynamic operating conditions [61].

Nevertheless, it can be deduced that this method is able to provide information about the development of the area specific cell resistance of the electrolysis cell without the need for additional impedance measurements, as the extracted *r*-values are within the same order of magnitude as those derived from the impedance spectra.

5. Results and discussion of PEM water electrolysis

In contrast to the operation of the AWE cells, we opted for a potentiodynamic operation for the PEM cells, as we had no problems with the recording of capacitive currents that generated overshoots or undershoots during potentiodynamic PEMWE measurements due to a different test rig setup and control and were thus able to stay in the potential limits of 1.45 V and 2 V.

After a break-in step described in 3.2.2, we first operated the PEMWE cells with the potentiodynamic wind profile (Figure S8, Supporting Information) without interruption for 350 h. Subsequently, the measurement was interrupted for 30 h during which we recorded I-V curves and impedance spectra. Thereafter, the measurement was continued with interruptions every 75 h to record I-V curves, which were used for comparison with the curves and resistance values extracted from dynamic data. One further impedance spectrum was recorded after 547 h. In the last quarter of the measurement additional unintentional interruptions occurred due to technical issues with the test bench.

5.1. Trigger level method – Temporal performance tracking of cell voltage changes

Fig. 9 summarizes the results of applying the trigger method to four current density levels of a dynamically operated PEMWE cell as described in Section 2. We applied a linear fit through all corresponding cell voltages to the current density levels under investigation from 24 h onwards. The gray dashed line marks the beginning of the fit. Based on Fig. 9(a), the evaluation using the trigger method for an individual PEMWE cell shows, that during uninterrupted dynamic operation the cell voltages exhibit a decreasing trend for current densities above $0.7\,A\,cm^{-2}$, indicating an increase in cell performance. A detailed analysis of smaller current densities (Figure S9, Supporting Information) reveals that the cell voltage changes for current densities below $0.58\,A\,cm^{-2}$ are slightly positive, up to $4.4 \pm 0.6\,\mu V\,h^{-1}$ at $0.1\,A\,cm^{-2}$. Another PEMWE cell in the test shows similar behavior with decreasing cell voltages above $0.58\,A\,cm^{-2}$ (Figure S9). Although the absolute values of the cell voltage changes were not exactly the same for different cells, trends and magnitudes were consistent. Additionally, we found that cell voltage changes are dependent on the current density level. Consequently, cell performance during dynamic operation does not deteriorate or improve across the entire current density range, but overvoltages change differently for smaller and higher current densities, as we also found for alkaline electrolysis. In the lower load range, the overvoltage is dominated by activation overvoltage [62], indicating that the activation overvoltage increases over time during dynamic operation when cell voltage changes are positive for small current

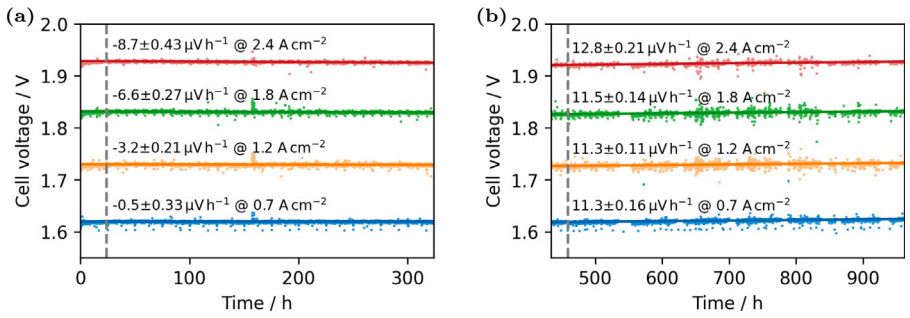

Fig. 9. Corresponding cell voltages for selected current density trigger levels with linear fit. a: First section of experiment without interruptions; b: Second section of experiment with interruptions. The horizontal dashed line marks the start of the fit at 24 h. Data from a PEMWE cell operated at 80.0 ± 1.0 °C end plate temperature.

densities. Alia et al. [6] also reported that performance losses during dynamic operation are dominated by kinetics, whereas resistance changes and transport losses had less influence on cell performance. On the other hand, opposing effects such as thinning of the membrane lead to a decrease in resistance and thus also to a decrease in cell voltage. However, thinning of the membrane can lead to pinhole formation in the long term and is therefore detrimental for the cell [8].

After 30 h of interruption for I-V curves and impedance spectra, increasing cell voltages were observed for all investigated current densities (Fig. 9(b)). Consequently, the trend of cell voltage changes in the second section of the experiment is reversed compared to the first uninterrupted section. Interruptions and cell potential drops to OCV can lead to changes in the morphology and oxidation state of iridium [63], resulting in iridium dissolution on the anode side, as well as particle agglomeration of platinum at the cathode side [26], and consequently to losses of active catalyst material. As some short and longer OCV phases occurred in this section of the experiment, losses of active catalyst material could be a reason for the aging rates in the second section of the experiment. The lowest degradation rate observed during interrupted dynamic operation was $11.30 \pm 0.16\,\mu V\,h^{-1}$ at $0.7\,A\,cm^{-2}$ and $1.2\,A\,cm^{-2}$ and the highest $12.8 \pm 0.2\,\mu V\,h^{-1}$ at $2.4\,A\,cm^{-2}$. These findings are in accordance with Alia et al. [6], where more pronounced cell voltage degradation at higher current densities were also found. We observed that cell voltage degradation was significantly lower within the first section of the experiment where dynamic operation was not interrupted than during dynamic operation with interruption as cell voltages even decreased during uninterrupted dynamic operation. If these trends were due to the mode of operation and not caused by the order in which the experiment was carried out, avoiding frequent interruptions could be beneficial for dynamically operated PEM water electrolyzers. On the other hand, load interruptions can lead to a short-term recovery of the cell voltage, as also described for alkaline electrolysis. In PEMWE, the effect of short-term recovery could be due to a structural change and change in the oxidation state of the iridium catalyst during a voltage drop from an metallic to a catalytically more active but more unstable amorphous phase [63]. However, the instability of the amorphous phase leads to increased iridium dissolution in the case of frequent interruptions and thus to a loss of catalytically active material in the long term. It is therefore possible that we observed cell voltage degradation in the second part of the experiment despite interruptions, which only lead to a short-term increase in performance. Further cell and stack tests are, as previously concluded for alkaline cells, required to confirm this hypothesis by reversing the test sections discussed here by first running dynamic operation with interruption followed by dynamic operation without interruption.

5.2. Surface fit method

For the application of the surface fit method, we used the same experimental data from PEMWE single cell tests as for the trigger method.

5.2.1. Temporal performance tracking of cell voltage changes

As with the trigger level method, cell voltage changes can be analyzed for different current density levels with the surface fit, as described in Section 2.2. Cross-sections of four current density levels are represented in Fig. 10 for the section of the experiment with and without interruptions. In addition, a small range of the measurement data around the surface fit is shown. Also displayed in Figs. 10(c) and 10(d) are the slopes of cell voltage changes as a function of the current density.

The cell voltage changes derived from the surface fit are close to those identified by the trigger level method, e.g., $-8.70 \pm 0.43\,\mu V\,h^{-1}$ from the trigger method and $-9.1 \pm 1.4\,\mu V\,h^{-1}$ from the surface fit at $2.4\,A\,cm^{-2}$ during uninterrupted operation. In the first section of the experiment without interruptions, all cell voltage changes above $0.4\,A\,cm^{-2}$ are negative, indicating cell performance improvement (Fig. 10(c)). The underlying effect here could be that within the first few hundred hours, the MEA adapts to the PTL, resulting in a better contact between PTL and catalyst layer. Consequently, more active catalyst sites are utilized and cell performance increases [7]. During the second section of the experiment with interruptions, shown in Fig. 10(b), all cell voltage changes are positive, as found by the trigger method, indicating losses in cell performance. The period for the output of the average slopes for the second section of the experiment starts at 459 h. In the second section of the experiment, average slopes determined from the trigger method range from $11.30 \pm 0.16\,\mu V\,h^{-1}$ to $12.80 \pm 0.21\,\mu V\,h^{-1}$ between $0.7\,A\,cm^{-2}$ and $2.4\,A\,cm^{-2}$. Average slopes determined from the surface fit range from $8.3 \pm 0.6\,\mu V\,h^{-1}$ to $6.3 \pm 1.3\,\mu V\,h^{-1}$ in the same current density range. The cell voltage changes are slightly different due to the segmentation of the surface fit, as well as the transition from positive to negative cell voltage changes in the low current density range described in Section 5.1 and S9. By creating a surface fit without segmentation with only one linear fit, analogous to the trigger method, the rates of change obtained using the two methods are almost identical (Figure S13), proving that the differences are due to the segmentation. Nevertheless, it is recommended to keep the segmentation of the surface fit to be able to monitor the temporal development of cell voltage changes, which is not implemented for the trigger method. However, due to the smaller computational effort and thus faster implementation, the use of the trigger method can be more practical depending on the application.

5.2.2. Extraction of I-V curves

During the second section of the experiment, we recorded nine I-V curves for comparison with the extracted I-V curves from the surface fit. The surface fit is shown in Fig. 11 and one example of an extracted I-V curve at 534 h of operation, compared to a recorded curve at the same time, is given in Fig. 11(b). More I-V curves from the surface plot are shown in the Supplementary Information (Figure S10). The root mean square error (RMSE) between the extracted and recorded curve always amounted to less than 7 mV and the average RMSE was 5 mV. Here, the RMSE between the recorded and extracted curve is used as

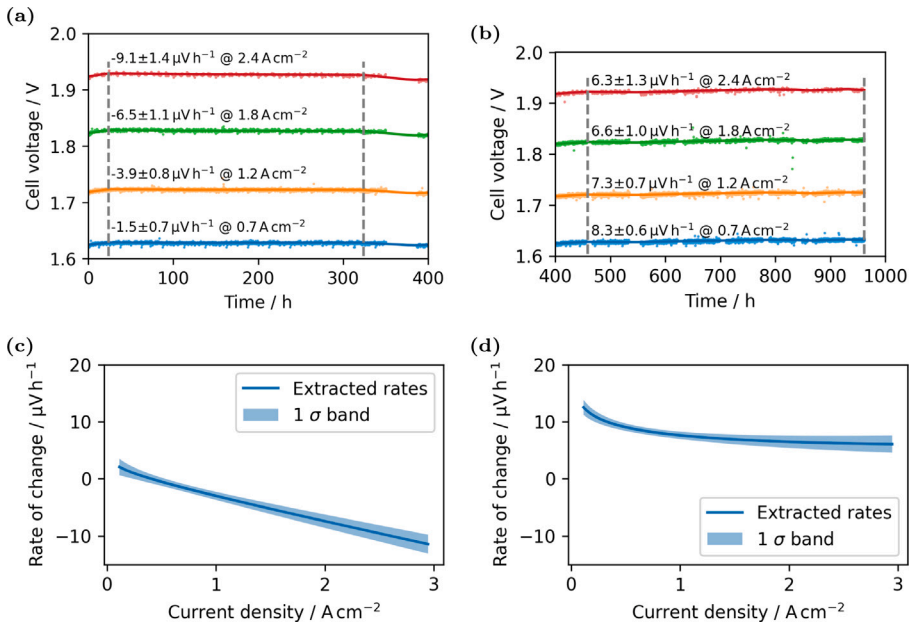

Fig. 10. Cell voltage changes with average slope of a PEMWE cell operated at 80.0 ± 1.0 °C end plate temperature for four selected current density levels extracted with the surface fit method, a: first section of the experiment without interruption; b: second section of the experiment with interruptions; c and d: cell voltage changes in dependence of current densities for the respective first and second section of the experiment. The horizontal dashed lines mark the start and end of the fit.

a measure for the difference between static and dynamic performance. Furthermore, the recorded I-V curves with an average spacing of 5 mV are sufficiently distinguishable from the distribution of the point cloud around the surface fit to confirm a real offset, as the data around the fit are on average distributed in a range of 1.4 mV. All recorded I-V curves are situated slightly below the extracted ones. This corresponds to our expectation, as the cell is not polarized for a short period of 20 s between the change from the dynamic measurement profile to the I-V curve recording. During this short load cutoff a regeneration takes place, that was already described in other studies [35,64]. The fact that the two curves are shifted parallel to each other but have the same shape implies two conclusions. One is an indication that the model of the surface fit realistically represents the shape of the I-V curve, and the other is an indication that the overvoltage, which causes the two curves to be shifted in parallel, is independent of the current density and thus not an ohmic overvoltage but, for example, a contribution by charge transfer overvoltage. Furthermore, the shift between the recorded and extracted curve shows that the performance of the electrolysis cells in dynamic operation does not correspond exactly to the performance displayed by slower recorded I-V curves. If an electrolyzer is to be operated dynamically, it is therefore consistent to specify a performance curve under dynamic conditions. The comparison of the curves underlines in addition that it is possible to obtain I-V curves during dynamic operation. Consequently, the performance of an electrolyzer can be tracked without interrupting its operation.

5.2.3. Development of ohmic cell resistances

To gain more information about the electrolyzer's state of health, usually impedance spectra are recorded, from which the ohmic cell resistance can be obtained in form of the high-frequency resistance. However, for large electrolyzers the recording of the impedance spectra is often not possible or technically complex due to high currents and low impedances [65]. These problems can be circumvented by extracting the fit parameter r from Eq. (4), representing the area-specific resistance. The resistances extracted from recorded and extracted I-V curves, as well as high-frequency resistances from three impedance spectra, are displayed in Fig. 12. The resistances determined from the recorded and extracted I-V curves differed less then 10 mΩ cm^2. Furthermore, the ohmic resistance remains stable and even decreases over time, supporting the assumption made above that losses in cell performance likely did not occur due to contributions to the ohmic resistance but rather due to other loss mechanisms not further elucidated. As Fig. 12 shows, the high-frequency resistances from EIS are very close to the values from the fit parameter r from the surface fit and the recorded curves. Consequently, our method is suitable for observing ohmic resistances from dynamically operated PEMWE where no impedance measurements can be carried out or interruptions must be avoided.

6. Conclusions

We created a realistic, semi-synthetic, high-resolution, and highly dynamic wind profile directly applicable as input profile for AWE and PEMWE single cells. Wind speed data forming the basis of the profile were combined with a 2 MW wind turbine model, while also considering terrain influences to create the power profile. This profile was then scaled down to work with single cells.

We propose two methods to analyze the I-V data from the operation of AWE and PEMWE cells with the wind profile. The trigger method is computationally lightweight and does not require a model of the current–voltage-relation of the electrolyzer. The surface fit method fits all available data points to a model instead of focusing on specific current levels which improves accuracy. It calculates plausible area resistances over time as fit parameters, which we validated with impedance spectroscopy. The surface fit method can also extract a spectrum of voltage change rates over current density, surpassing conventional methods by providing uniquely detailed insight into the voltage change aspect of the aging process.

By analyzing cell voltage changes at different current density levels, we found that the cell voltage degradation rates depend on current density and mode of operation, meaning that cell voltage changes at low, intermediate and high current densities are different. This distribution of the rates of change can provide information about the development of activation- and ohmic overvoltages and thus indicate the localization of aging effects of the catalyst layer or metallic components, being an important building block in aging analysis.

Experiments ran for up to 961 h and were split in parts with and without interruptions. During interruptions we recorded I-V curves

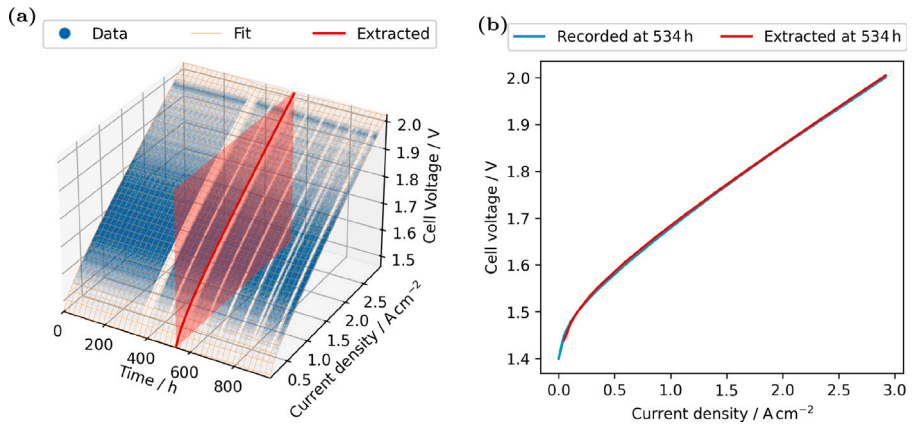

Fig. 11. Left: 3D I-V data point cloud of a PEMWE cell operated at 80.0 ± 1.0 °C end plate temperature, surface fit as wire frame and extracted I-V curve with a cross-sectional plane; right: example of a time cut at 534 h of the surface fit giving the extracted I-V curve, comparison with a recorded curve.

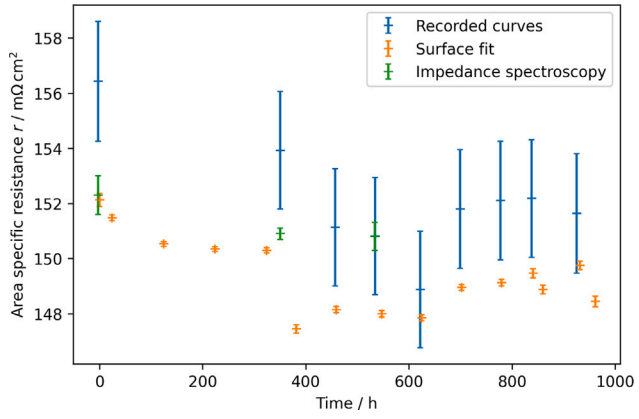

Fig. 12. Development of the ohmic resistance from fit to the recorded curves (blue), fit to the dynamic data (orange), and high frequency resistances from impedance spectra (green). Data from a PEMWE cell that was operated at 80.0 ± 1.0 °C end plate temperature. (For interpretation of the references to color in this figure legend, the reader is referred to the web version of this article.)

and performed impedance spectroscopy which we compare to results form our methods such as I-V curves, cell voltage changes, and ohmic resistances. Small differences are most likely due to measuring slightly different properties than the reference methods, i.e. dynamic operation compared to equilibrium operation.

For the first time, our methods enable the extraction of these performance parameters from uninterrupted highly dynamic operation. These major advancements help avoid the distortions of the aging process caused by the interruptions and help pave the way for the analysis of highly dynamically operated electrolyzers in combination with renewable energy sources.

CRediT authorship contribution statement

Sharon-Virginia Pape: Writing – original draft, Validation, Methodology, Investigation, Formal analysis, Data curation, Conceptualization. **Sarah Zerressen:** Writing – original draft, Validation, Methodology, Investigation, Formal analysis, Data curation, Conceptualization. **Martin Florian Seidler:** Writing – original draft, Visualization, Software, Methodology, Conceptualization. **Roger Keller:** Writing – original draft, Methodology. **Felix Lohmann-Richters:** Writing – review & editing, Supervision, Funding acquisition, Conceptualization. **Martin Müller:** Writing – review & editing, Funding acquisition, Conceptualization. **Ulf-Peter Apfel:** Writing – review & editing, Supervision. **Anna K. Mechler:** Writing – review & editing, Supervision. **Andreas Glüsen:** Writing – review & editing, Supervision, Funding acquisition, Conceptualization.

Declaration of competing interest

The authors declare that they have no known competing financial interests or personal relationships that could have appeared to influence the work reported in this paper.

Acknowledgments

We acknowledge financial support by the German Federal Ministry of Economic Affairs and Climate Action (BMWK) for the project “NextH2” under grant agreement No. 03EI3011A-C. Furthermore, this research was funded by the European project TELEGRAM, part of the European Union’s Horizon 2020 Research and Innovation Program under grant agreement No. 101006941. The work was also funded by the German Federal Ministry of Education and Research (BMBF) in the framework of the project “Wasserstoff: Elektrolyse – Elektrochemische Wasserstofferzeugung der nächsten Generation (HyInnoLyze)”, grant agreement 03 ZU 1115 AA. This work is transferred to be used within the Korea Institute of Energy Technology Evaluation and Planning (KETEP) grant funded by the Korea government (MOTIE) (RS-2023-00303610). Open access funding is provided by the Deutsche Forschungsgemeinschaft (DFG, German Research Foundation) – 491111487.

Appendix A. Supplementary data

Supplementary material related to this article can be found online at https://doi.org/10.1016/j.ijhydene.2025.03.387.

Data availability

The data that support the findings of this study and the Python code used for analysis are openly available in Jülich Data [66].

References

[1] Franchi G, Capocelli M, de Falco M, Piemonte V, Barba D. Hydrogen production via steam reforming: A critical analysis of MR and RMM technologies. Membranes 2020;10(1). http://dx.doi.org/10.3390/membranes10010010.

[2] Falcone PM, Hiete M, Sapio A. Hydrogen economy and sustainable development goals: Review and policy insights. Curr Opin Green Sustain Chem 2021;31:100506. http://dx.doi.org/10.1016/j.cogsc.2021.100506.

[3] Capurso T, Stefanizzi M, Torresi M, Camporeale SM. Perspective of the role of hydrogen in the 21st century energy transition. Energy Convers Manage 2022;251:114898. http://dx.doi.org/10.1016/j.enconman.2021.114898.

[4] Zhang F, Zhao P, Niu M, Maddy J. The survey of key technologies in hydrogen energy storage. Int J Hydrog Energy 2016;41(33):14535–52. http://dx.doi.org/10.1016/j.ijhydene.2016.05.293.

[5] Ehlers JC, Feidenhans'l AA, Therkildsen KT, Larrazábal GO. Affordable green hydrogen from alkaline water electrolysis: Key research needs from an industrial perspective. ACS Energy Lett 2023;8(3):1502–9. http://dx.doi.org/10.1021/acsenergylett.2c02897.

[6] Alia SM, Stariha S, Borup RL. Electrolyzer durability at low catalyst loading and with dynamic operation. J Electrochem Soc 2019;166(15):F1164–72. http://dx.doi.org/10.1149/2.0231915jes.

[7] Rakousky C, Reimer U, Wippermann K, Kuhri S, Carmo M, Lueke W, Stolten D. Polymer electrolyte membrane water electrolysis: Restraining degradation in the presence of fluctuating power. J Power Sources 2017;342:38–47. http://dx.doi.org/10.1016/j.jpowsour.2016.11.118.

[8] Frensch SH, Fouda-Onana F, Serre G, Thoby D, Araya SS, Kæ r SK. Influence of the operation mode on PEM water electrolysis degradation. Int J Hydrog Energy 2019;44(57):29889–98. http://dx.doi.org/10.1016/j.ijhydene.2019.09.169.

[9] Brauns J, Turek T. Alkaline water electrolysis powered by renewable energy: A review. Processes 2020;8(2):248. http://dx.doi.org/10.3390/pr8020248.

[10] Ansar AS, Gago AS, Razmjooei F, Reißner R, Xu Z, Friedrich KA. Alkaline electrolysis—status and prospects. In: Electrochemical power sources: Fundamentals, systems, and applications. Elsevier; 2022, p. 165–98. http://dx.doi.org/10.1016/B978-0-12-819424-9.00004-5.

[11] Brauns J, Turek T. Experimental evaluation of dynamic operating concepts for alkaline water electrolyzers powered by renewable energy. Electrochim Acta 2022;404:139715. http://dx.doi.org/10.1016/j.electacta.2021.139715.

[12] Smolinka T, Ojong ET, Garche J. Hydrogen production from renewable energies—Electrolyzer technologies. In: Electrochemical energy storage for renewable sources and grid balancing. Elsevier; 2015, p. 103–28. http://dx.doi.org/10.1016/B978-0-444-62616-5.00008-5.

[13] Kojima H, Nagasawa K, Todoroki N, Ito Y, Matsui T, Nakajima R. Influence of renewable energy power fluctuations on water electrolysis for green hydrogen production. Int J Hydrog Energy 2023;48(12):4572–93. http://dx.doi.org/10.1016/j.ijhydene.2022.11.018.

[14] Yde L, Kjartansdóttir C, Allebrod F, Mogensen M, Møller P, Hilbert L, Nielsen P, Mathiesen T, Jensen J, Andersen L, Dierking A. 2nd generation alkaline electrolysis: Final report. Århus University Business and Social Science – Centre for Energy Technologies; 2013, URL https://orbit.dtu.dk/en/publications/2nd-generation-alkaline-electrolysis-final-report, EUDP 63011-0200.

[15] Bertuccioli L, Chan A, Hart D, Lehner F, Madden B, Standen E. Development of water electrolysis in the European union: Final report. 2014, URL https://www.clean-hydrogen.europa.eu/system/files/2014-09/study%2520electrolyser_0-Logos_0_0.pdf.

[16] Hug W, Divisek J, Mergel J, Seeger W, Stee H. Highly efficient advanced alkaline electrolyzer for solar operation. Int J Hydrog Energy 1992;17(9):699–705. http://dx.doi.org/10.1016/0360-3199(92)90090-J.

[17] Nakajima Y, Fujimoto N, Hasegawa S, Usui T. Advanced alkaline water electrolyzer for renewable hydrogen production. ECS Trans 2017;80(10):835–41. http://dx.doi.org/10.1149/08010.0835ecst.

[18] Divisek J, Mergel J, Schmitz H. Advanced water electrolysis and catalyst stability under discontinuous operation. Int J Hydrog Energy 1990;15(2):105–14. http://dx.doi.org/10.1016/0360-3199(90)90032-T.

[19] Schiller G. High performance electrodes for an advanced intermittently operated 10-kw alkaline water electrolyzer. Int J Hydrog Energy 1998;23(9):761–5. http://dx.doi.org/10.1016/S0360-3199(97)00122-5.

[20] Ayers K. The potential of proton exchange membrane–based electrolysis technology. Curr Opin Electrochem 2019;18:9–15. http://dx.doi.org/10.1016/j.coelec.2019.08.008.

[21] Lee H, Lee B, Byun M, Lim H. Economic and environmental analysis for PEM water electrolysis based on replacement moment and renewable electricity resources. Energy Convers Manage 2020;224:113477. http://dx.doi.org/10.1016/j.enconman.2020.113477.

[22] Barbir F. PEM electrolysis for production of hydrogen from renewable energy sources. Sol Energy 2005;78(5):661–9. http://dx.doi.org/10.1016/j.solener.2004.09.003.

[23] Crespi E, Guandalini G, Mastropasqua L, Campanari S, Brouwer J. Experimental and theoretical evaluation of a 60 kW PEM electrolysis system for flexible dynamic operation. Energy Convers Manage 2023;277:116622. http://dx.doi.org/10.1016/j.enconman.2022.116622.

[24] Tofighi-Milani M, Fattaheian-Dehkordi S, Lehtonen M. Dynamic response analysis of alkaline and PEM electrolyzers in low-inertia power systems: A comparative study. In: 2024 IEEE international conference on environment and electrical engineering and 2024 IEEE industrial and commercial power systems europe (EEEIC / i&cPS europe). 2024, p. 01–6. http://dx.doi.org/10.1109/EEEIC/ICPSEurope61470.2024.10750998.

[25] Sayed-Ahmed H, Toldy Á, Santasalo-Aarnio A. Dynamic operation of proton exchange membrane electrolyzers—Critical review. Renew Sustain Energy Rev 2024;189:113883. http://dx.doi.org/10.1016/j.rser.2023.113883, URL https://www.sciencedirect.com/science/article/pii/S1364032123007414.

[26] Brightman E, Dodwell J, van Dijk N, Hinds G. In situ characterisation of PEM water electrolysers using a novel reference electrode. Electrochem Commun 2015;52:1–4. http://dx.doi.org/10.1016/j.elecom.2015.01.005.

[27] Weiß A, Siebel A, Bernt M, Shen T-H, Tileli V, Gasteiger HA. Impact of intermittent operation on lifetime and performance of a PEM water electrolyzer. J Electrochem Soc 2019;166(8):F487–97. http://dx.doi.org/10.1149/2.0421908jes.

[28] Berlin H. HTW berlin weather data with a temporal resolution of 1 hz and 1/60 hz (2017–2020). 2020, URL https://wetter.htw-berlin.de/Home/Info.

[29] L. MM. An induction-aware parameterization for wind farms in the WRF mesoscale model. In: 1618 062006, 2020, http://dx.doi.org/10.1088/1742-6596/1618/6/062006,

[30] Spiru P, Simona PL. Wind energy resource assessment and wind turbine selection analysis for sustainable energy production. Sci Rep 2024;14(1):10708. http://dx.doi.org/10.1038/s41598-024-61350-6.

[31] Lopez-Villalobos CA, Martínez-Alvarado O, Rodriguez-Hernandez O, Romero-Centeno R. Analysis of the influence of the wind speed profile on wind power production. Energy Rep 2022;8:8079–92. http://dx.doi.org/10.1016/j.egyr.2022.06.046.

[32] Anjum L. Wind resource estimation techniques-an overview. Int J Wind Renew Energy 2014;3(2):26–38, URL https://www.researchgate.net/profile/lalit-anjum/publication/305806761_wind_resource_estimation_techniques-an_overview/links/57a21cd408aeb1604834aa2b/wind-resource-estimation-techniques-an-overview.pdf.

[33] Fernández-Guillamón A, Gómez-Lázaro E, Muljadi E, Molina-García Á. Power systems with high renewable energy sources: A review of inertia and frequency control strategies over time. Renew Sustain Energy Rev 2019;115:109369. http://dx.doi.org/10.1016/j.rser.2019.109369.

[34] Virtanen P, Gommers R, Oliphant TE, Haberland M, Reddy T, Cournapeau D, Burovski E, Peterson P, Weckesser W, Bright J, van der Walt SJ, Brett M, Wilson J, Millman KJ, Mayorov N, Nelson ARJ, Jones E, Kern R, Larson E, Carey CJ, Polat İ, Feng Y, Moore EW, VanderPlas J, Laxalde D, Perktold J, Cimrman R, Henriksen I, Quintero EA, Harris CR, Archibald AM, Ribeiro AH, Pedregosa F, van Mulbregt P. SciPy 1.0: fundamental algorithms for scientific computing in Python. 1548- 7105 2020;17(3):261–72. http://dx.doi.org/10.1038/s41592-019-0686-2, URL https://www.nature.com/articles/s41592-019-0686-2.

[35] Rakousky C. Langzeitstabilität der polymerelektrolyt-wasserelektrolyse bei reduziertem iridiumgehalt. Schriften des Forschungszentrums Jülich: Reihe Energie & Umwelt, Band 322, Jülich: Forschungszentrum Jülich GmbH, Zentralbibliothek, Verlag; 2016.

[36] Puranen P, Hehemann M, Kütemeier P, Järvinen L, Ruuskanen V, Kosonen A, Ahola J, Kauranen P. Using the nonlinearity of a PEM water electrolyzer cell for its dynamic model characterization. 2024, http://dx.doi.org/10.2139/ssrn.4809803.

[37] de Groot MT, Vreman AW. Ohmic resistance in zero gap alkaline electrolysis with a zirfon diaphragm. Electrochim Acta 2021;369:137684. http://dx.doi.org/10.1016/j.electacta.2020.137684.

[38] Karacan C, Lohmann-Richters FP, Keeley GP, Scheepers F, Shviro M, Müller M, Carmo M, Stolten D. Challenges and important considerations when benchmarking single-cell alkaline electrolyzers. Int J Hydrog Energy 2022;47(7):4294–303. http://dx.doi.org/10.1016/j.ijhydene.2021.11.068.

[39] Hodges A, Renz S, Lohmann-Richters F, Al-Musawi A, Jupke A, Lehnert W, Swiegers GF, Wallace GG. Critical analysis of published physical property data for aqueous potassium hydroxide. Collation into detailed models for alkaline electrolysis. J Chem Eng Data 2023;68(7):1485–506. http://dx.doi.org/10.1021/acs.jced.3c00040.

[40] de Groot MT. Alkaline water electrolysis: with or without iron in the electrolyte? Curr Opin Chem Eng 2023;42:100981. http://dx.doi.org/10.1016/j.coche.2023.100981.

[41] Demnitz M, Lamas YM, Garcia Barros RL, de Leeuw den Bouter A, van der Schaaf J, Theodorus de Groot M. Effect of iron addition to the electrolyte on alkaline water electrolysis performance. IScience 2024;27(1):108695. http://dx.doi.org/10.1016/j.isci.2023.108695.

[42] Ranz M, Grabner B, Schweighofer B, Wegleiter H, Trattner A. Dynamics of anion exchange membrane electrolysis: Unravelling loss mechanisms with electrochemical impedance spectroscopy, reference electrodes and distribution of relaxation times. J Power Sources 2024;605:234455. http://dx.doi.org/10.1016/j.jpowsour.2024.234455.

[43] Lickert T, Fischer S, Young JL, Klose S, Franzetti I, Hahn D, Kang Z, Shviro M, Scheepers F, Carmo M, Smolinka T, Bender G, Metz S. Advances in benchmarking and round robin testing for PEM water electrolysis: Reference protocol and hardware. Appl Energy 2023;352:121898. http://dx.doi.org/10.1016/j.apenergy.2023.121898, URL https://www.sciencedirect.com/science/article/pii/S030626192301262X.

[44] Tsotridis G, Pilenga A. EU harmonized protocols for testing of low temperature water electrolysis. In: EUR, vol. 30752, Luxembourg: Publications Office of the European Union; 2021.

[45] Pourbaix M. Atlas of electrochemical equilibria in aqueous solutions. Houston, Texas, USA: NACE International Cebelcor; 1974.
[46] Rocha F, de Radiguès Q, Thunis G, Proost J. Pulsed water electrolysis: A review. Electrochim Acta 2021;377:138052. http://dx.doi.org/10.1016/j.electacta.2021.138052.
[47] Huot J-Y, Brossard L. In situ activation of nickel cathodes by sodium molybdate during alkaline water electrolysis at constant current. J Appl Electrochem 1990;20(2):281–8. http://dx.doi.org/10.1007/BF01033606.
[48] Rommal HEG, Morgan PJ. The role of absorbed hydrogen on the voltage–time behavior of Nickel cathodes in hydrogen evolution. J Electrochem Soc 1988;135(2):343–6. http://dx.doi.org/10.1149/1.2095612.
[49] Rommal HEG, Moran PJ. Time–dependent energy efficiency losses at Nickel cathodes in alkaline water electrolysis systems. J Electrochem Soc 1985;132(2):325–9. http://dx.doi.org/10.1149/1.2113831.
[50] Soares DM, Teschke O, Torriani I. Hydride effect on the kinetics of the hydrogen evolution reaction on Nickel cathodes in alkaline media. J Electrochem Soc 1992;139(1):98–105. http://dx.doi.org/10.1149/1.2069207.
[51] Huot J, Brossard L. Time dependence of the hydrogen discharge at 70°C on nickel cathodes. Int J Hydrog Energy 1987;12(12):821–30. http://dx.doi.org/10.1016/0360-3199(87)90103-0.
[52] Abouatallah RM, Kirk DW, Graydon JW. Long-term electrolytic hydrogen permeation in nickel and the effect of vanadium species addition. Electrochim Acta 2002;47(15):2483–94. http://dx.doi.org/10.1016/S0013-4686(02)00108-1.
[53] Pierozynski B. On the hydrogen evolution reaction at Nickel-coated carbon fibre in 30 wt. % KOH solution. Int J Electrochem Sci 2011;6(1):63–77. http://dx.doi.org/10.1016/S1452-3981(23)14975-3.
[54] Sayed DM, El-Nagar GA, Sayed SY, El-Anadouli BE, El-Deab MS. Activation/deactivation behavior of nano-niox based anodes towards the OER: Influence of temperature. Electrochim Acta 2018;276:176–83. http://dx.doi.org/10.1016/j.electacta.2018.04.175.
[55] Lu PWT, Srinivasan S. Electrochemical–Ellipsometric studies of oxide film formed on Nickel during oxygen evolution. J Electrochem Soc 1978;125(9):1416–22. http://dx.doi.org/10.1149/1.2131689.
[56] Conway BE, Angerstein-Kozlowska H, Sattar MA, Tilak BV. Study of a decomposing hydride phase at Nickel cathodes by measurement of open–circuit potential decay. J Electrochem Soc 1983;130(9):1825–36. http://dx.doi.org/10.1149/1.2120106.
[57] Janjua M, Leroy R. Electrocatalyst performance in industrial water electrolysers. Int J Hydrog Energy 1985;10(1):11–9. http://dx.doi.org/10.1016/0360-3199(85)90130-2.
[58] Agfa. Technical data sheet: Zirfon perl UTP 220. 2021, URL https://www.agfa.com/specialty-products/solutions/membranes/request-your-zirfon-utp-220-tds/.
[59] Zuo Y, Bellani S, Ferri M, Saleh G, Shinde DV, Zappia MI, Brescia R, Prato M, de Trizio L, Infante I, Bonaccorso F, Manna L. High-performance alkaline water electrolyzers based on ru-perturbed cu nanoplatelets cathode. Nat Commun 2023;14(1):4680. http://dx.doi.org/10.1038/s41467-023-40319-5.
[60] Ali MF, Cho H-S, Bernäcker CI, Albers J, Young-Woo C, Kim M, Lee JH, Lee C, Lee S, Cho W-C. A study on the effect of TiO2 nanoparticle size on the performance of composite separators in alkaline water electrolysis. J Membr Sci 2023;678:121671. http://dx.doi.org/10.1016/j.memsci.2023.121671.
[61] Lira Garcia Barros R, Kelleners MH, van Bemmel L, van der Leegte TV, van der Schaaf J, de Groot MT. Elucidating the increased ohmic resistances in zero-gap alkaline water electrolysis. Electrochim Acta 2024;507:145161. http://dx.doi.org/10.1016/j.electacta.2024.145161.
[62] Taie Z, Peng X, Kulkarni D, Zenyuk IV, Weber AZ, Hagen C, Danilovic N. Pathway to complete energy sector decarbonization with available iridium resources using ultralow loaded water electrolyzers. ACS Appl Mater & Interfaces 2020;12(47):52701–12. http://dx.doi.org/10.1021/acsami.0c15687.
[63] Bernt M, Hartig-Weiß A, Tovini MF, El-Sayed HA, Schramm C, Schröter J, Gebauer C, Gasteiger HA. Current challenges in catalyst development for PEM water electrolyzers. Chem Ing Tech 2020;92(1–2):31–9. http://dx.doi.org/10.1002/cite.201900101.
[64] Parra-Restrepo J. Characterization of aging and operating heterogeneities within a proton exchange electrolyzer (PEM) electrolyzer: caractérisation des hétérogénéités de fonctionnement et de dégradation au sein d'un électrolyseur à membrane échangeuse de protons (PEM) (Ph.D. thesis), Université de Lorraine; 2020, URL https://hal.univ-lorraine.fr/tel-02942062.
[65] Krenz T, Gottschalk T, Helmers L, Trinke P, Bensmann B, Hanke-Rauschenbach R. Current interrupt technique to fully characterize PEMWE cells. J Electrochem Soc 2024;171(3):034509. http://dx.doi.org/10.1149/1945-7111/ad3057.
[66] Zerressen S, Pape S-V, Seidler F. Data from dynamic wind profile long-term operation of alkaline and PEM water electrolysis with extraction of performance data in Python. 2024, http://dx.doi.org/10.26165/JUELICH-DATA/PYGQTO.